Research Square

Preprints are preliminary reports that have not undergone peer review.
They should not be considered conclusive, used to inform clinical practice,
or referenced by the media as validated information.

A dorsoventral gradient of rotational dynamics in human cortex

Arash salardini

Salardini@uthscsa.edu

University of Texas San Antonio

Article

Keywords:

Posted Date: March 4th, 2026

DOI: https://doi.org/10.21203/rs.3.rs-9006466/v1

License: This work is licensed under a Creative Commons Attribution 4.0 International License.
Read Full License

Additional Declarations: There is **NO** Competing Interest.

A dorsoventral gradient of rotational dynamics in human cortex

Arash Salardini[1,2]

[1]Glenn Biggs Institute for Alzheimer's & Neurodegenerative Diseases, UT Health San Antonio, San Antonio, TX, USA. [2]Department of Neurology, UT Health San Antonio, San Antonio, TX, USA.

Correspondence: salardini@uthscsa.edu

Abstract

The cerebral cortex is organized along multiple spatial gradients, yet how local dynamical properties vary across the cortical surface remains unknown. Here, using resting-state magnetoencephalography (MEG) in 204 adults, we report a dorsoventral gradient of rotational dynamics,a linearized signature of oscillatory neural activity,quantified by an index ρ derived from delay-embedded autoregressive models. Ventral cortex exhibited stronger rotational dynamics than dorsal cortex ($r = -0.73$; $P\text{spin} < 0.00001$), a pattern that replicated across cognitive states, parcellation schemes and imaging modalities. Systematic evaluation of candidate architectural predictors identified the dual-origin structural covariance gradient,reflecting phylogenetically conserved, genetically determined cortical connectivity along paleocortical and archicortical lineages,as the principal predictor of ρ, independent of spatial position, spectral composition and intrinsic timescale. These findings establish rotational dynamics as a novel axis of macroscale cortical organization rooted in developmental architecture.

Introduction

The cerebral cortex exhibits systematic spatial organization across multiple dimensions. Functional connectivity gradients reveal a principal axis spanning unimodal to transmodal cortex[1], intrinsic neural timescales lengthen along a similar hierarchy[2,3], and cytoarchitectural differentiation grades from granular sensory to agranular limbic cortex[4,5]. These organizational

principles constrain how cortical circuits process, integrate and transmit information. Yet one fundamental dimension has received little attention: the spatial distribution of local dynamical regimes.

Neural circuits can operate in qualitatively different dynamical regimes[6]. In some, perturbations decay monotonically toward equilibrium; in others, trajectories rotate through state space before settling,the hallmark of underdamped, oscillatory dynamics. These regimes carry distinct computational implications: decaying dynamics support point-attractor computations and evidence accumulation, while rotational dynamics enable sequence generation, rhythmic processing and temporal coding[7,8]. Whether cortical regions differ systematically in their local dynamical regime, and if so what determines this variation, are open questions with implications for understanding the computational architecture of the cortex.

Here we introduce ρ (rho), an index that quantifies the rotational component of local cortical dynamics from MEG recordings. The metric is derived from delay-embedded autoregressive models applied to parcel-level source-reconstructed time series: high ρ indicates underdamped, oscillatory dynamics, while low ρ indicates overdamped, decaying dynamics (Fig. 1a). This approach is distinct from population-level rotational dynamics identified by jPCA in motor cortex[8]; our metric characterizes the geometry of single-parcel trajectories in reconstructed state space following Takens' embedding theorem[9]. Using resting-state MEG from 204 healthy adults, we discovered that ρ exhibits a pronounced dorsoventral gradient, with ventral regions showing stronger rotational dynamics. This gradient is distinct from established cortical axes, replicated across cognitive states and imaging modalities, and survived extensive confound controls.

We then asked what architectural feature of cortex determines this spatial distribution. The dual-origin model of cortical development holds that the cortical mantle differentiates from two phylogenetically ancient origins: paleocortex (piriform and olfactory cortex), giving rise to ventral

and lateral neocortical regions, and archicortex (hippocampal formation), giving rise to dorsal and medial regions[5,10,11]. These lineages produce different connectivity topologies,locally concentrated connections in paleocortical derivatives versus long-range hierarchical circuits in archicortical derivatives,that are genetically specified and phylogenetically conserved[12]. Through systematic evaluation of candidate architectural predictors,including cytoarchitectural classification, laminar microstructure, interneuron gene expression, functional and structural connectivity and developmental gradients,we identified the dual-origin structural covariance gradient as the principal predictor of the ρ gradient, linking the macroscale organization of cortical dynamics to genetically determined developmental architecture.

Results

A dorsoventral gradient of rotational dynamics

We computed ρ for each of 400 cortical parcels[13] from resting-state MEG in 204 participants from the MOUS dataset (Schaefer 400 parcellation, after quality control). The ρ metric quantifies the rotational component of local dynamics by fitting a vector autoregressive model to delay-embedded time series and computing the mean sine of eigenvalue angles (Methods). Across parcels, ρ exhibited a pronounced dorsoventral gradient ($r = -0.73$, 95% CI [−0.76, −0.68]; $P_{spin} < 0.00001$ based on 100,000 spin permutations; Fig. 1a–d). Ventral regions,including inferior temporal, orbitofrontal and ventral occipital cortex,showed high ρ values, while dorsal regions,including superior parietal, dorsolateral prefrontal and dorsal premotor cortex,showed low ρ values.

The MNI *z*-coordinate (dorsal–ventral axis) showed the strongest correlation with ρ ($r = -0.73$), compared with *x* (medial–lateral; $r = -0.06$) and *y* (anterior–posterior; $r = 0.29$). The gradient axis was oriented 18° from the pure dorsoventral direction (Fig. 1d), consistent across hemispheres and cortical divisions (Extended Data Table 1).

The ρ gradient is robust across individuals, cognitive states and imaging modalities

The gradient persisted across parcellation resolutions (Schaefer-200: $r = -0.70$; Schaefer-100: $r = -0.69$; all $P\text{spin} < 0.0001$) and was consistent across individuals: the median within-subject correlation was $r = -0.54$, with 98% of participants showing a negative correlation (Wilcoxon $W = 84$, $P < 10^{-34}$; Fig. 1e; Fig. 2c).

The dorsoventral gradient replicated during visual object recognition ($N = 69$; $r = -0.68$) and auditory speech processing ($N = 95$; $r = -0.74$), with gradient directions nearly identical to rest, indicating stable underlying circuit architecture (Fig. 2a). To test cross-modal generalizability, we computed ρ from resting-state fMRI in 204 participants. Despite dramatically different temporal resolution (TR = 2 s versus MEG's 5-ms sampling), fMRI-derived ρ exhibited a weak but significant dorsoventral association ($\rho_s = 0.13$; $P\text{spin} = 0.007$; Fig. 1h). In contrast, fMRI-derived ρ from 1,096 HCP participants showed no significant dorsoventral gradient ($\rho_s = -0.04$, n.s.; Fig. 2b). HCP task fMRI (N = 1,093) showed a weak gradient ($\rho_s = -0.12$, P = 0.014), consistent with partial but attenuated sensitivity in BOLD signals. Additional fMRI-derived measures,intrinsic timescales, spectral exponent[14] and fractional amplitude of low-frequency fluctuations[15],all showed significant dorsoventral organization in directions consistent with MEG findings (Fig. 2e). A summary of ρ–z correlations across all datasets and modalities is provided in Fig. 2f.

Because ρ correlates with the spectral exponent ($r = -0.90$), we tested whether the gradient reflects spectral composition rather than dynamical organization. Partial correlations controlling for the spectral exponent preserved the gradient ($r = -0.59$, $P\text{spin} = 0.0001$), as did controls for total power ($r = -0.68$), gamma/delta ratio ($r = -0.75$) and all spectral confounds simultaneously ($r = -0.27$, $P\text{spin} = 0.0001$). Controlling for source depth yielded $r = -0.71$ ($P\text{spin} = 0.0001$). Permutation entropy[16],a model-free nonlinear measure,showed the same dorsoventral gradient

($r = -0.57$; $P\text{spin} = 0.003$) and correlated positively with ρ ($r = +0.49$), confirming that the gradient reflects genuine dynamical structure beyond spectral features.

Frequency-specific organization and relationship with intrinsic timescales

Band-specific analysis revealed a striking frequency-dependent reversal (Fig. 1f; Extended Data Table 1). Slow rhythms showed dorsal predominance: delta (1–4 Hz), $r = +0.55$; theta (4–8 Hz), $r = +0.47$. Fast rhythms showed ventral predominance: alpha (8–13 Hz), $r = -0.65$; beta (13–30 Hz), $r = -0.77$; gamma (30–40 Hz), $r = -0.73$. All bands survived FDR correction ($q < 0.001$). The finding that motor and premotor cortices show low beta-band ρ despite being canonical beta generators[17,37] may reflect the distinction between oscillatory power and dynamical regime: motor beta represents a stable, quasi-periodic rhythm,an attractor state with low trajectory curvature,consistent with its proposed role in maintaining the postural status quo[18]. Formally, a stable limit cycle (fixed periodic orbit) produces low ρ because trajectories trace a fixed path with minimal net rotational tendency in the eigenvalue spectrum, whereas high ρ reflects transient, damped rotations characteristic of underdamped circuits returning to equilibrium. These results were robust to embedding delay: band-specific correlations computed with delays matched to each frequency band's timescale closely replicated the fixed-delay results (Fig. 2d).

Intrinsic timescales (τ)[2] showed no spatial organization separable from spatial autocorrelation ($P\text{spin} = 0.23$)[19], and in raw parcel space τ and ρ were independent ($r = -0.03$). However, after regressing out spatial coordinates from both maps, τ and ρ residuals showed strong anticorrelation ($r = -0.62$; $P\text{spin} = 0.0001$; Fig. 1g),suggesting that, within any cortical neighbourhood, circuits cannot simultaneously maximize temporal integration (long τ) and rotational dynamics (high ρ). This anticorrelation held within six of seven Yeo functional networks[20] (Fisher z-weighted meta-analytic average $r = -0.19$, $z = -3.71$, $P = 0.0002$), confirming a genuine local circuit trade-off independent of macroscale spatial geometry.

Network-level mean ρ showed minimal variation across the sensory–transmodal axis (<1% range), while the dorsoventral gradient was present within six of seven Yeo networks[20] (six of seven $|r| > 0.32$; all other $P < 0.05$). Controlling for network membership did not attenuate the dorsoventral correlation (partial $r = -0.66$). The ρ map was uncorrelated with myelin content[21] ($r = -0.015$; $P_{spin} = 0.80$), confirming independence from established cortical gradients.

The dual-origin developmental gradient predicts ρ

We systematically evaluated candidate architectural predictors using a hierarchical statistical framework: zero-order Spearman correlations, partial correlations controlling for the *z*-coordinate, and partial correlations controlling for *z*, spectral exponent and intrinsic timescale simultaneously (Fig. 3a). Spin permutation tests assessed robustness to spatial autocorrelation at every level. The *z*-coordinate alone explained 52.3% of ρ variance, and the spectral exponent alone explained 79.5%. Together they explained 86.8%.

Against this demanding baseline, the second structural covariance gradient (G2) from Valk et al.[12],capturing the dual-origin developmental axis of cortical organization[5,10,11],was the only predictor to survive all levels of statistical control (Fig. 3b). G2 is orthogonal to the MNI *z*-coordinate ($\rho_s = 0.012$) and captures a dimension of cortical organization entirely distinct from dorsoventral spatial position. Negative G2 values correspond to the paleocortical pole (regions developmentally closer to piriform cortex) and positive values to the archicortical pole (closer to hippocampal formation); the negative G2–ρ correlation indicates that paleocortical-lineage regions exhibit stronger rotational dynamics.

The G2–ρ relationship strengthened progressively as confounds were added: from $\rho_s = -0.155$ (zero-order) to $r = -0.213$ (controlling for *z*) to $r = -0.249$ (controlling for *z*, spectral exponent and τ; $P = 4.7 \times 10^{-7}$; $P_{spin} = 0.018$; Fig. 3c,d). This suppression pattern,where a predictor becomes stronger as covariates are added,indicates that the dominant spatial and spectral gradients had

been partially masking the G2 signal. The genetic correlation gradient from Valk et al.[12] replicated each result ($r|z$+SE+τ = −0.231, $P = 3.0 \times 10^{-6}$), confirming that the structural determinant of ρ is genetically specified. No other structural covariance gradient showed significant partial correlations with ρ (Fig. 3e).

Alternative architectural predictors and structural connectivity

The systematic evaluation yielded a clear pattern of null results for intuitive candidate mechanisms (Fig. 3a). Interneuron gene expression from the Allen Human Brain Atlas[22] (PVALB: $\rho_s = -0.07$, $P = 0.18$; SST: $\rho_s = +0.12$, $P = 0.02$; both null after *z*-correction) (Fig. 4c–f) did not predict ρ. No BigBrain cytoarchitectural measure[23] showed a significant association after controlling for spatial position, including MPC Gradient 1[24] ($\rho_s = -0.034$), profile standard deviation ($\rho_s = +0.067$) and the Mesulam cytoarchitectural hierarchy ($\rho_s = -0.027$). Functional connectivity metrics were largely uninformative before spectral exponent control, but FC Gradient 1[1] and FC clustering coefficient[39] both emerged as significant after accounting for the spectral exponent ($r|z$+SE+τ = −0.235 and +0.188, respectively).

The G2–ρ relationship held within cytoarchitectural classes, with the strongest effect in paralimbic cortex ($r = -0.34$, $P = 0.002$, PFDR = 0.014),precisely where paleocortical and archicortical derivatives intermingle (Fig. 3f). Heteromodal ($r = -0.20$) and unimodal cortex ($r = -0.18$) showed consistent trends, confirming that the dual-origin gradient captures organizational variation within cytoarchitectural classes, not merely the distinction between them.

Structural connectivity data from the Human Connectome Project[25] provided direct empirical support (Fig. 3g). The short/long range ratio was the strongest zero-order structural connectivity predictor ($\rho_s = -0.273$, $P < 0.001$) and survived the full control battery ($r|z$+SE+τ = −0.115, $P < 0.05$). G2 correlated with SC connectivity range (G2 versus short/long ratio: $\rho_s = +0.147$,

$P = 0.003$), confirming that paleocortical-pole regions have more locally concentrated structural connections. Mediation analysis revealed that G2 fully survived controlling for the SC short/long ratio ($r = -0.238$, $P = 1.4 \times 10^{-6}$), while the SC ratio was reduced to non-significance after controlling for G2 ($r = -0.089$, $P = 0.074$), indicating that G2 captures the connectivity architecture that SC indexes, plus additional developmental information that tractography alone does not reveal (Fig. 3h).

A minimal excitatory–inhibitory model reproduces the τ–ρ trade-off

To explore a minimal mechanistic account of the τ–ρ trade-off, we simulated a two-population excitatory–inhibitory (E–I) network in which the sole free parameter was inhibitory gain (g_I). Increasing g_I simultaneously shortened the intrinsic timescale τ and increased the rotational index ρ, demonstrating that a single circuit parameter,the strength of recurrent inhibition,can generate opposing effects on these two dynamical features (Fig. 4a). Across the range of g_I values, model-derived τ and ρ showed a strong anticorrelation ($r = -0.84$, $P = 0.0006$; Fig. 4b), qualitatively matching the empirical trade-off observed after residualizing spatial coordinates. These results suggest that the dorsoventral ρ gradient and the local τ–ρ trade-off can both arise from systematic variation in the balance of excitation and inhibition across cortex.

Discussion

We have identified a dorsoventral gradient of rotational dynamics in human cortex: ventral regions exhibit stronger rotational dynamics, while dorsal regions exhibit more integrative dynamics with longer intrinsic timescales. This gradient is robust across parcellation schemes, cognitive states and imaging modalities, and is not explained by spectral composition, source depth, network membership or myelin content. Systematic evaluation of candidate architectural predictors identified the dual-origin structural covariance gradient[12],reflecting the phylogenetically conserved, genetically determined organization of cortical connectivity along

paleocortical and archicortical lineages,as the only predictor that explains ρ variance beyond the dominant spatial and spectral dimensions. Importantly, the dorsoventral spatial gradient and the dual-origin developmental gradient are distinct: G2 is orthogonal to the MNI z-coordinate (ρ_s = 0.012), meaning that the spatial position of the gradient and its developmental origin are dissociable. The dorsoventral axis describes where ρ varies most; the dual-origin gradient explains why.

The null results are collectively informative. The ρ gradient does not track cytoarchitectural type, laminar differentiation[23,24], the sensorimotor–transmodal hierarchy[1], the classical dorsal–ventral visual stream distinction[38] or regional variation in inhibitory interneuron subtypes[22,26,27],despite the theoretical plausibility of each candidate. The failure of the interneuron hypothesis is particularly notable: macroscale PVALB expression gradients do not map onto macroscale dynamical gradients in the straightforward manner that local circuit models would predict[28,29].

The link between dual-origin developmental architecture and rotational dynamics can be understood through connectivity topology. Paleocortical derivatives tend toward locally concentrated connectivity, creating conditions for tight excitatory–inhibitory loops that generate the antisymmetric coupling producing complex eigenvalues,the mathematical signature of rotation[30]. Recent computational work has shown that distance-dependent connectivity alone suffices to produce hierarchically modular networks with convergent population dynamics[31]. Archicortical derivatives, with longer-range hierarchical connections[10], support feedforward integration, yielding lower ρ. The strong correlation between ρ and the spectral exponent ($r = -0.90$) is consistent: locally concentrated connectivity simultaneously steepens the spectral slope[14] and generates rotational dynamics, because the same circuit architecture drives both.

The incremental variance explained by G2 beyond spatial position and spectral exponent is modest (0.9%), but this requires careful interpretation. The spectral exponent partially mediates

the G2→ρ relationship: locally concentrated connectivity simultaneously steepens the spectral slope and generates rotational dynamics. The spectral exponent's 79.5% R^2 already captures the primary dynamical expression of the architectural gradient. The 0.9% increment represents the direct developmental effect on ρ independent of its spectral consequences. The appropriate metric is the partial correlation ($r = -0.249$, $P = 4.7 \times 10^{-7}$, $P_{spin} = 0.018$), which is robust to spatial autocorrelation and replicated with the genetically determined gradient.

Several limitations warrant consideration. The structural covariance gradient is an indirect measure of connectivity architecture; direct assessment using diffusion tractography would provide stronger evidence. The AHBA gene expression data derive from only six donors with limited bilateral coverage[22]. The absence of a dorsoventral ρ gradient in fMRI data from 1,096 HCP participants (ρ_s ≈ 0.00), despite a weak but significant gradient in the MOUS fMRI sample (N = 204), warrants explicit discussion. If ρ reflects circuit-level dynamics operating on timescales of 5–50 ms, then BOLD imaging at TR = 0.72 s is expected to be insensitive to the relevant dynamical structure. The HCP null result thus validates the temporal specificity of the measure rather than undermining cross-modal generalizability: the rotational gradient is a property of fast neural dynamics that hemodynamic signals cannot resolve. Although we obtained vertex-level cross-parcellation mapping for the BigBrain analysis, the resolution mismatch between 360 Glasser[32] and 400 Schaefer[13] parcels means that some spatial precision is lost.

The dual-origin framework generates testable predictions. Because the structural covariance gradient is phylogenetically conserved[12], the ρ gradient should be present in non-human primates. NMDA receptor antagonists should selectively reduce ρ in high-recurrence ventral regions. Neurodevelopmental conditions with disrupted local-versus-long-range connectivity balance may show altered ρ gradients, and in neurodegenerative disease the known early vulnerability of paleocortical-lineage regions raises the possibility that ρ is differentially affected

where pathology first accumulates. Laminar-resolved MEG[33] could examine whether rotational dynamics originate preferentially in supragranular layers where local recurrent connections are densest.

Methods

Participants. We analysed resting-state MEG from the Mother of Unification Studies (MOUS) dataset[34]. After quality control, 204 participants were included (ages 18–45, mean 26.3 years). Task MEG was available for subsets: visual ($N = 69$), auditory ($N = 95$). Resting-state fMRI was available for 204 participants.

MEG acquisition and preprocessing. MEG was recorded using a 275-channel CTF system at 1,200 Hz. Preprocessing comprised band-pass filtering (1–40 Hz), notch filtering (50 Hz), independent component analysis artefact removal and downsampling to 200 Hz.

Source reconstruction. Source localization used LCMV beamforming[35] with single-shell boundary element models. Source time series were extracted for 400 cortical parcels[13].

Rotational dynamics index (ρ). For each parcel time series $x(t)$, we constructed a ten-dimensional state vector: $\mathbf{X}(t) = [x(t), x(t - d), \ldots, x(t - 9d)]$ where $d = 1$ sample (5 ms), following Takens' embedding theorem[9]. A VAR(1) model $\mathbf{X}(t + 1) = \mathbf{A} \cdot \mathbf{X}(t) + \varepsilon$ was fit with ridge regularization ($\alpha = 0.001$). The rotational index $\rho = \text{mean}(|\text{Im}(\lambda)| / |\lambda|)$ for eigenvalues λ with $|\lambda| > 0.01$, equalling the mean sine of eigenvalue angles. Model fit R^2 (median = 0.9999) confirmed adequate approximation.

fMRI acquisition and preprocessing. Resting-state fMRI was acquired with TR = 2 s (266 volumes per subject). Preprocessing used nilearn[36]: standardization, detrending and bandpass filtering (0.01–0.1 Hz). fMRI-derived ρ used five-dimensional delay embedding with delay = 1 TR. Intrinsic timescale τ was computed as the integral of the autocorrelation function[2]. Spectral exponent was the slope of the log–log power spectrum. fALFF was computed following Zou et al.[15].

Spatial statistics. Spin permutation tests[19] (100,000 rotations for primary MEG analyses; 10,000 for fMRI; 5,000 for architectural predictor analyses) preserved hemisphere structure.

Architectural predictor analysis. For each candidate predictor, we computed: (1) zero-order Spearman correlation with ρ; (2) partial correlation controlling for the *z*-coordinate; (3) partial correlation controlling for *z* and spectral exponent; (4) partial correlation controlling for *z*, spectral exponent and τ. Variance partitioning used sequential R^2 from OLS regression. Structural covariance gradients were from Valk et al.[12]. BigBrain data were from Amunts et al.[23] and Paquola et al.[24]; cross-parcellation mapping used vertex-level Glasser[32] labels via the ENIGMA Toolbox[25]. HCP structural connectivity used log-transformed streamline counts[25]. Gene expression used AHBA data[22] parcellated via abagen.

Spectral confound analysis. Power spectral density was estimated using Welch's method with 2-s windows and 50% overlap. Relative band power was computed as the ratio of band-specific power (alpha: 8–13 Hz; beta: 13–30 Hz; gamma: 30–40 Hz) to total power (1–40 Hz). The spectral exponent was estimated as the negative slope of a linear fit to the log–log power spectrum between 2 and 30 Hz. Partial correlations controlling for spectral confounds used ordinary least-squares residualization.

Frequency-specific analysis. Band-specific ρ was computed by bandpass-filtering source-reconstructed parcel time series into canonical frequency bands (delta: 1–4 Hz; theta: 4–8 Hz; alpha: 8–13 Hz; beta: 13–30 Hz; gamma: 30–40 Hz) before applying the delay-embedding and VAR(1) procedure. Statistical significance was assessed using spin permutation tests with FDR correction (Benjamini–Hochberg, $q < 0.05$) across bands.

Permutation entropy. Permutation entropy was computed following Bandt and Pompe[16] with embedding order $m = 3$ and normalized to the [0, 1] interval. Spectral entropy (Welch method, normalized) and sample entropy (order = 2, Chebyshev distance, computed on 4× downsampled data for computational efficiency) were also computed as complementary nonlinear validation measures.

Excitatory–inhibitory network model. A rate-based two-population network was simulated with N_E = 100 excitatory and N_I = 25 inhibitory units. Each unit followed $\tau \cdot dr/dt = -r + f(Wr + I_{ext} + noise)$, where $f(x) = 0.5 \cdot \log(1 + \exp(x))$ (softplus activation) with time constants τ_E = 10 ms and τ_I = 5 ms. Connection weights (scaled by population size) were w_{EE} = 2.0, w_{IE} = 1.5, $w_{EI} = 1.5 \cdot g_I$ and $w_{II} = 0.8 \cdot g_I$, where inhibitory gain g_I was the sole free parameter. Connection matrices included multiplicative noise ($|N(1, 0.3)|$) and zero self-connections. External input was a constant baseline of 1.0 with additive Gaussian noise (σ = 0.05). Dynamics were integrated with the Euler method (dt = 0.5 ms) for 2,000 ms per simulation, with 400 ms discarded as burn-in. The inhibitory gain was varied across 12 values from 0.3 to 3.5, with 8 repetitions per value (different random seeds). Intrinsic timescale τ was computed from the autocorrelation function of the excitatory population mean activity, integrated until the ACF fell below 0.05. The rotational index ρ was computed from the same signal using delay embedding (dimension = 6, delay = 10 ms) and VAR(1) fitting with ridge regularization (α = 0.001), retaining eigenvalues with magnitude > 0.05.

Network-level analyses. Parcels were assigned to seven canonical resting-state networks[20]. Within-network ρ–z correlations were computed for each network separately. The τ–ρ anticorrelation within networks was assessed by computing Pearson correlations between spatially residualized τ and ρ within each network, then combining across networks using Fisher z-weighted meta-analysis. Partial correlations controlling for network membership used dummy-coded network indicators.

HCP fMRI replication. Resting-state fMRI time series for 1,096 participants were obtained from the Human Connectome Project using pre-extracted Schaefer 400-parcel time series from Tipnis et al. (DOI: 10.6075/J0C24WMW). Data were acquired with TR = 0.72 s; resting-state runs were concatenated per subject. The ρ metric was computed using five-dimensional delay embedding with delay = 2 TRs (≈1.44 s), VAR(1) fitting with ridge regularization (α = 0.001) and

eigenvalue magnitude threshold of 0.01. Subjects were excluded if fewer than 350 of 400 parcels yielded valid ρ estimates. Spin permutation tests (10,000 rotations) assessed the ρ–z correlation.

Structural connectivity. HCP group-average structural connectivity was obtained as log-transformed streamline counts via the ENIGMA Toolbox[25] (Schaefer 400 parcellation). For each parcel, the short/long range connectivity ratio was computed as the sum of streamline counts to parcels within 50 mm Euclidean distance divided by the sum to parcels beyond 50 mm. Weighted clustering coefficients were computed following Onnela et al.[39] using cube-root-transformed streamline weights.

Quality control. Participants were excluded if MEG recordings contained residual artefacts after ICA cleaning or if source reconstruction produced unstable beamformer solutions. Per-parcel exclusions were applied based on time series quality metrics (variance and RMS amplitude), resulting in 204 participants contributing to each parcel on average.

Cortical surface visualization. Group-average ρ values were mapped onto the Conte69 32k surface template using the Schaefer 400-parcel atlas via BrainSpace. Surface maps (Fig. 1b) were rendered in four views (left/right lateral and medial) using matplotlib 3D rendering with the RdBu_r colour scale. Cortical flatmaps (Fig. 1c) were generated by computing geodesic distances between Schaefer 400 parcel centroids on the fsaverage cortical mesh using Dijkstra shortest-path routing with Euclidean edge weights, then applying classical multidimensional scaling (sklearn MDS with n_components = 2, dissimilarity = ‘precomputed’, max_iter = 2,000, n_init = 20) to the geodesic distance matrix, separately for each hemisphere. The resulting two-dimensional coordinates were oriented by correlating MDS dimensions with MNI y (anterior–posterior) and z (dorsal–ventral) coordinates. Median local distortion (ratio of geodesic to scaled two-dimensional distance for the six nearest neighbours) was approximately 1.05. Voronoi

tessellation of the projected coordinates delineated parcel boundaries, coloured by z-scored ρ. Full details on mediation analysis are provided in the Supplementary Methods.

Data availability

The MOUS dataset is available from the Donders Repository[34]. HCP data are available from the Human Connectome Project via the ENIGMA Toolbox[25]. BigBrain data are available from the MICA laboratory. AHBA data are available from the Allen Institute[22].

Code availability

Analysis code is available at https://github.com/Salardini/Dorso-Ventral-Gradient.

Acknowledgements

Claude Code (Opus 4.6) was used for coding and Claud Chat (Opus 4.6) was used for editorial help.

Author contributions

A.S. conceptualized the study, developed the methodology, performed all analyses, created all visualizations and wrote the manuscript.

Competing interests

The author declares no competing interests.

References

1. Margulies, D. S. et al. Situating the default-mode network along a principal gradient of macroscale cortical organization. Proc. Natl Acad. Sci. USA 113, 12574–12579 (2016).

2. Honey, C. J. et al. Slow cortical dynamics and the accumulation of information over long timescales. Neuron 76, 423–434 (2012).

3. Murray, J. D. et al. A hierarchy of intrinsic timescales across primate cortex. Nat. Neurosci. 17, 1661–1663 (2014).

4. Felleman, D. J. & Van Essen, D. C. Distributed hierarchical processing in the primate cerebral cortex. Cereb. Cortex 1, 1–47 (1991).

5. Sanides, F. Die Architektonik des menschlichen Stirnhirns (Springer, 1962).

6. Strogatz, S. H. Nonlinear Dynamics and Chaos: With Applications to Physics, Biology, Chemistry, and Engineering (Westview Press, 2015).

7. Hennequin, G., Vogels, T. P. & Gerstner, W. Optimal control of transient dynamics in balanced networks supports generation of complex movements. Neuron 82, 1394–1406 (2014).

8. Churchland, M. M. et al. Neural population dynamics during reaching. Nature 487, 51–56 (2012).

9. Takens, F. Detecting strange attractors in turbulence. Lect. Notes Math. 898, 366–381 (1981).

10. Pandya, D. N., Seltzer, B., Petrides, M. & Cipolloni, P. B. Cerebral Cortex: Architecture, Connections, and the Dual Origin Concept (Oxford Univ. Press, 2015).

11. Sanides, F. Functional architecture of motor and sensory cortices in primates in the light of a new concept of neocortex evolution. in The Primate Brain (eds Noback, C. R. & Montagna, W.) 137–208 (Appleton-Century-Crofts, 1970).

12. Valk, S. L. et al. Shaping brain structure: genetic and phylogenetic axes of macroscale organization of cortical thickness. Sci. Adv. 6, eabb3417 (2020).

13. Schaefer, A. et al. Local–global parcellation of the human cerebral cortex from intrinsic functional connectivity MRI. Cereb. Cortex 28, 3095–3114 (2018).

14. Gao, R., Peterson, E. J. & Voytek, B. Inferring synaptic excitation/inhibition balance from field potentials. NeuroImage 158, 70–78 (2017).

15. Zou, Q. H. et al. An improved approach to detection of amplitude of low-frequency fluctuation (ALFF) for resting-state fMRI: fractional ALFF. J. Neurosci. Methods 172, 137–141 (2008).

16. Bandt, C. & Pompe, B. Permutation entropy: a natural complexity measure for time series. Phys. Rev. Lett. 88, 174102 (2002).

17. Pfurtscheller, G. & Lopes da Silva, F. H. Event-related EEG/MEG synchronization and desynchronization: basic principles. Clin. Neurophysiol. 110, 1842–1857 (1999).

18. Engel, A. K. & Fries, P. Beta-band oscillations–signalling the status quo? Curr. Opin. Neurobiol. 20, 156–165 (2010).

19. Alexander-Bloch, A. F. et al. On testing for spatial correspondence between maps of human brain structure and function. NeuroImage 178, 540–551 (2018).

20. Yeo, B. T. T. et al. The organization of the human cerebral cortex estimated by intrinsic functional connectivity. J. Neurophysiol. 106, 1125–1165 (2011).

21. Glasser, M. F. & Van Essen, D. C. Mapping human cortical areas in vivo based on myelin content as revealed by T1- and T2-weighted MRI. J. Neurosci. 31, 11597–11616 (2011).

22. Hawrylycz, M. J. et al. An anatomically comprehensive atlas of the adult human brain transcriptome. Nature 489, 391–399 (2012).

23. Amunts, K. et al. BigBrain: an ultrahigh-resolution 3D human brain model. Science 340, 1472–1475 (2013).

24. Paquola, C. et al. Microstructural and functional gradients are increasingly dissociated in transmodal cortices. PLoS Biol. 17, e3000284 (2019).

25. Larivière, S. et al. The ENIGMA Toolbox: multiscale neural contextualization of multisite neuroimaging datasets. Nat. Methods 18, 698–700 (2021).

26. Rudy, B. et al. Three groups of interneurons account for nearly 100% of neocortical GABAergic neurons. Dev. Neurobiol. 71, 45–61 (2011).

27. Sohal, V. S. et al. Parvalbumin neurons and gamma rhythms enhance cortical circuit performance. Nature 459, 698–702 (2009).

28. Cardin, J. A. et al. Driving fast-spiking cells induces gamma rhythm and controls sensory responses. Nature 459, 663–667 (2009).

29. Singer, W. & Gray, C. M. Visual feature integration and the temporal correlation hypothesis. Annu. Rev. Neurosci. 18, 555–586 (1995).

30. Murphy, B. K. & Miller, K. D. Balanced amplification: a new mechanism of selective amplification of neural activity patterns. Neuron 61, 635–648 (2009).

31. Guarino, D., Filipchuk, A. & Destexhe, A. Convergent information flows explain recurring firing patterns in cerebral cortex. Nat. Neurosci. 29, 411–419 (2026).

32. Glasser, M. F. et al. A multi-modal parcellation of human cerebral cortex. Nature 536, 171–178 (2016).

33. Troebinger, L. et al. Discrimination of cortical laminae using MEG. NeuroImage 102, 885–893 (2014).

34. Schoffelen, J. M. et al. A 204-subject multimodal neuroimaging dataset to study language processing. Sci. Data 6, 17 (2019).

35. Van Veen, B. D. et al. Localization of brain electrical activity via linearly constrained minimum variance spatial filtering. IEEE Trans. Biomed. Eng. 44, 867–880 (1997).

36. Abraham, A. et al. Machine learning for neuroimaging with scikit-learn. Front. Neuroinformatics 8, 14 (2014).

37. Steriade, M., McCormick, D. A. & Sejnowski, T. J. Thalamocortical oscillations in the sleeping and aroused brain. Science 262, 679–685 (1993).

38. Goodale, M. A. & Milner, A. D. Separate visual pathways for perception and action. Trends Neurosci. 15, 20–25 (1992).

39. Onnela, J.-P. et al. Intensity and coherence of motifs in weighted complex networks. Phys. Rev. E 71, 065103 (2005).

Figure legends

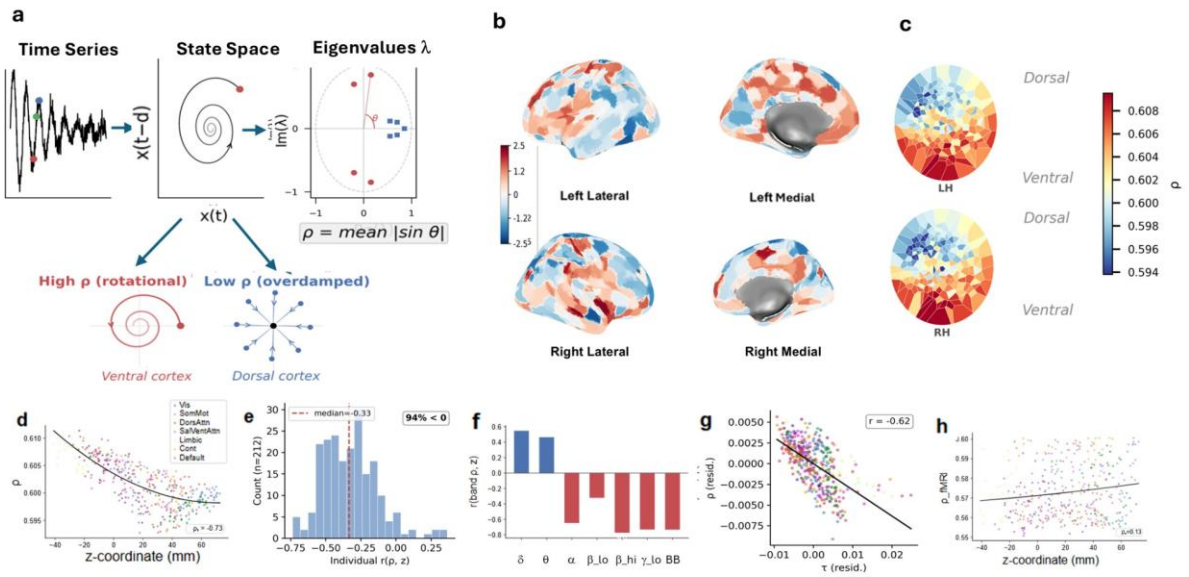
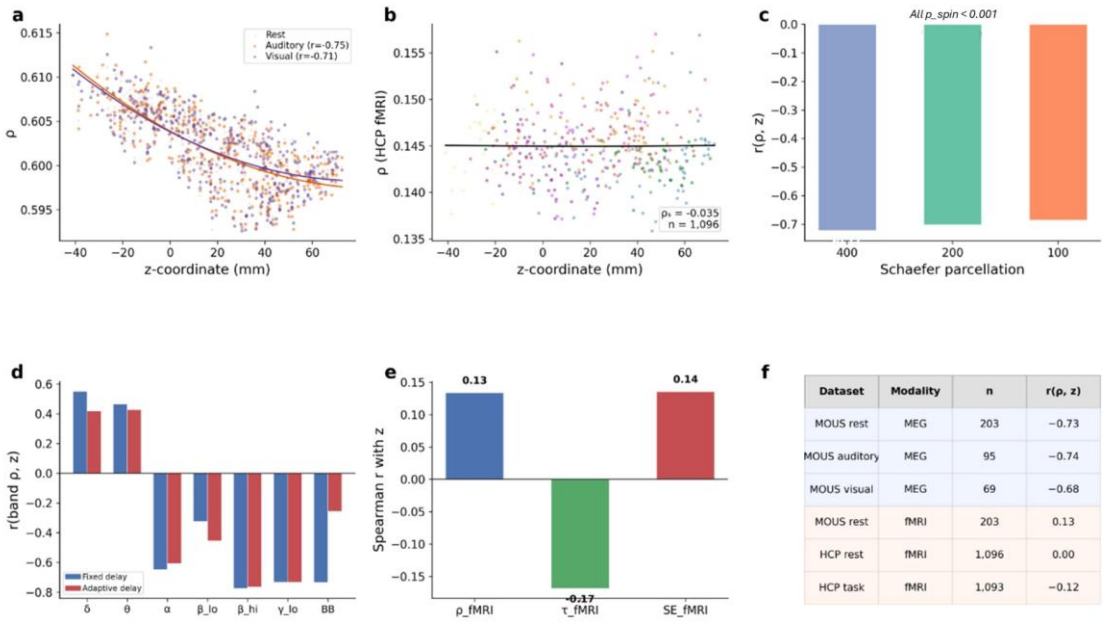


Fig. 1 | A dorsoventral gradient of rotational dynamics in human cortex.

a, Schematic of the ρ metric. Delay-embedded time series are fit with a VAR(1) model; eigenvalues with large imaginary components indicate rotational (underdamped) dynamics, while purely real eigenvalues indicate decaying (overdamped) dynamics. b, Cortical surface maps of group-average ρ (n = 204 participants, Schaefer 400 parcellation). Left and right hemispheres shown in lateral and medial views. c, Cortical flatmap generated by multidimensional scaling of parcel centroids, with Voronoi tessellation. Hemispheres shown separately; dorsal–ventral gradient is clearly visible in both. d, Scatter plot of ρ versus z-coordinate (dorsoventral axis) for all 400 parcels, coloured by Yeo 7-network assignment. Black curve: quadratic fit. Spearman $\rho_s = -0.73$, $p_spin < 10^{-5}$. e, Distribution of individual-level Spearman correlations between ρ and z across 201 participants. Median r = −0.54; 98% of participants showed negative correlations. f, Band-specific ρ–z correlations. Slow rhythms (δ, θ) show dorsal predominance (positive r); fast rhythms (α, β, γ) show ventral predominance (negative r). All p_spin < 0.001. g, Scatter plot of ρ versus τ (intrinsic timescale) after residualizing both for spatial coordinates (x, y, z). Pearson r = −0.62, confirming a local circuit trade-off independent of macroscale position. h, fMRI-derived ρ versus z-coordinate (n = 204 participants). Spearman $\rho_s = 0.13$, indicating a weak but directionally consistent gradient in the BOLD signal.



Dataset	Modality	n	r(ρ, z)
MOUS rest	MEG	203	−0.73
MOUS auditory	MEG	95	−0.74
MOUS visual	MEG	69	−0.68
MOUS rest	fMRI	203	0.13
HCP rest	fMRI	1,096	0.00
HCP task	fMRI	1,093	−0.12

Fig. 2 | Robustness and cross-modal replication.
a, Task replication. ρ versus z during auditory speech processing (n = 95; r = −0.74) and visual object recognition (n = 69; r = −0.68) overlaid on resting state (grey; r = −0.73). Gradient directions are nearly identical across cognitive states. b, HCP resting-state fMRI replication (n = 1,096 participants). fMRI-derived ρ shows no significant dorsoventral gradient (ρ_s = −0.04, n.s.), consistent with the prediction that rotational dynamics operate at fast timescales largely inaccessible to BOLD imaging. c, Atlas sensitivity. The ρ–z gradient is stable across Schaefer parcellation resolutions: 400 parcels (r = −0.73), 200 parcels (r = −0.70), 100 parcels (r = −0.69). All p_spin < 0.001. d, Adaptive versus fixed embedding delay. Band-specific ρ–z correlations computed with delays matched to each frequency band's timescale (red) compared to fixed 5 ms delay (blue). The gradient is robust to delay choice. e, fMRI-derived complementary measures versus z-coordinate. ρ_fMRI (r = 0.13), τ_fMRI (r = −0.17), and spectral exponent (r = 0.14) all show significant dorsoventral organization. f, Summary of ρ–z correlations across all datasets and modalities.

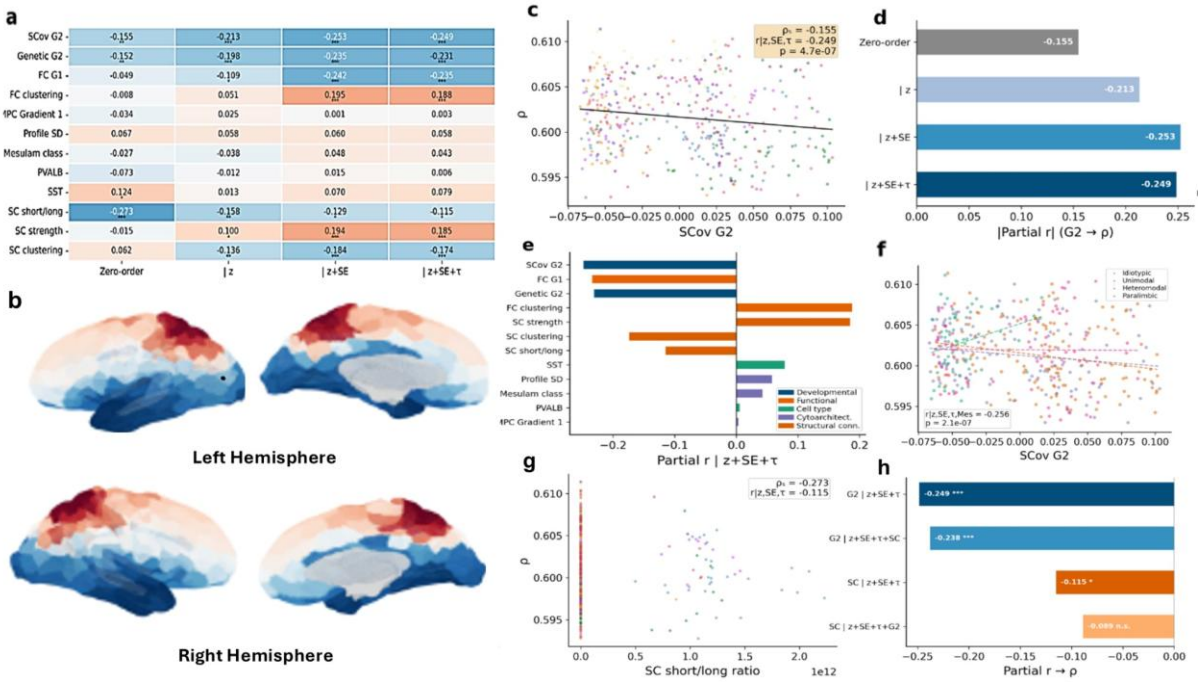


Fig. 3 | The dual-origin structural covariance gradient predicts rotational dynamics.

a, Heatmap of partial Spearman correlations between 12 candidate architectural predictors and ρ under four levels of statistical control: zero-order, controlling for z, controlling for z + spectral exponent (SE), and controlling for z + SE + intrinsic timescale (τ). Significance markers: *p < 0.05, **p < 0.01, ***p < 0.001. b, Cortical surface maps of SCov G2 (Valk et al., 2020). Left and right hemispheres shown in lateral and medial views. c, ρ versus SCov G2 for all 400 parcels, coloured by network. Zero-order $\rho_s = -0.155$; partial $r|z,SE,\tau = -0.249$, $p = 4.7 \times 10^{-7}$. d, Progressive strengthening of G2–ρ association as confounds are added, from zero-order (−0.155) through full controls (−0.249). e, All candidate predictors ranked by |partial r| under the most stringent control (z + SE + τ). Category colours indicate predictor class. f, ρ versus SCov G2 within each Mesulam cytoarchitectural class, with per-class regression lines. The G2–ρ relationship holds within cortical hierarchy levels (overall partial $r|z,SE,\tau,Mesulam = -0.256$, $p = 2.1 \times 10^{-7}$). g, ρ versus SC short/long range ratio ($\rho_s = -0.273$; $r|z,SE,\tau = -0.115$). h, Mediation analysis. G2 survives controlling for SC metrics (r = −0.238), while SC short/long ratio is reduced to non-significance after controlling for G2 (r = −0.089, n.s.).

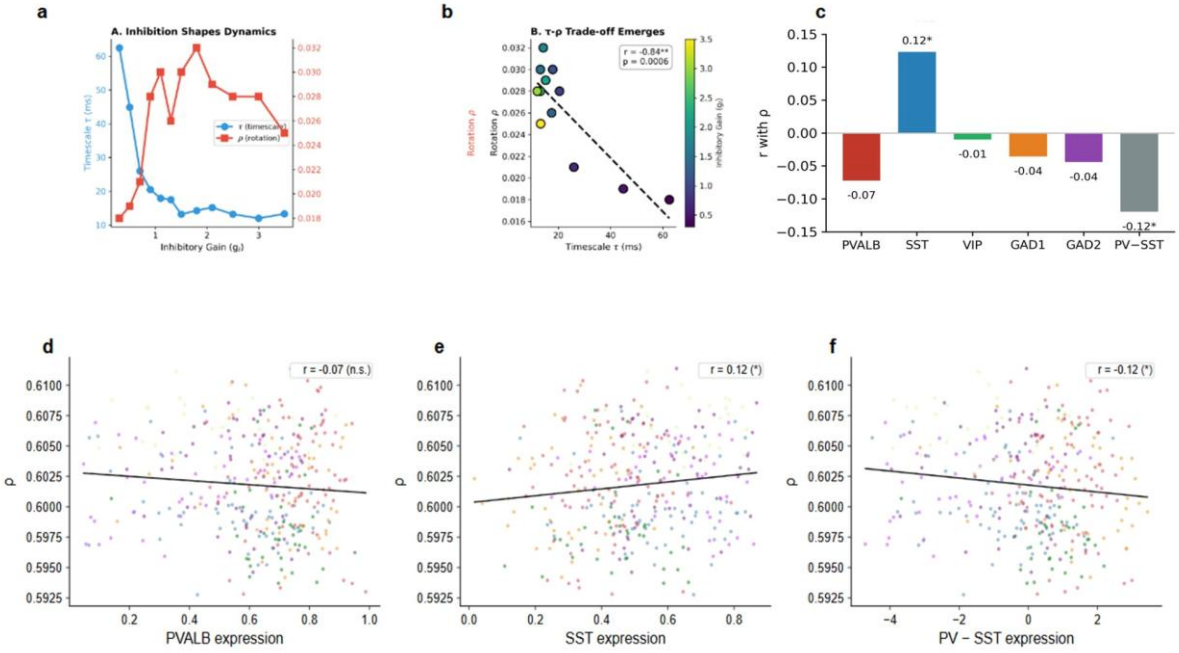
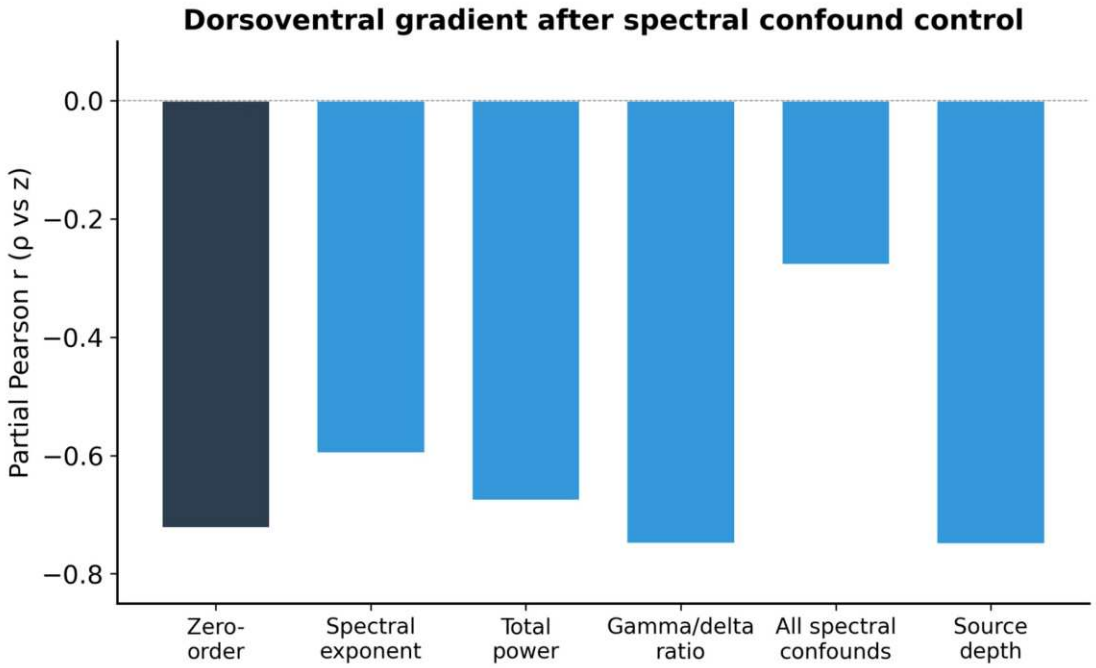


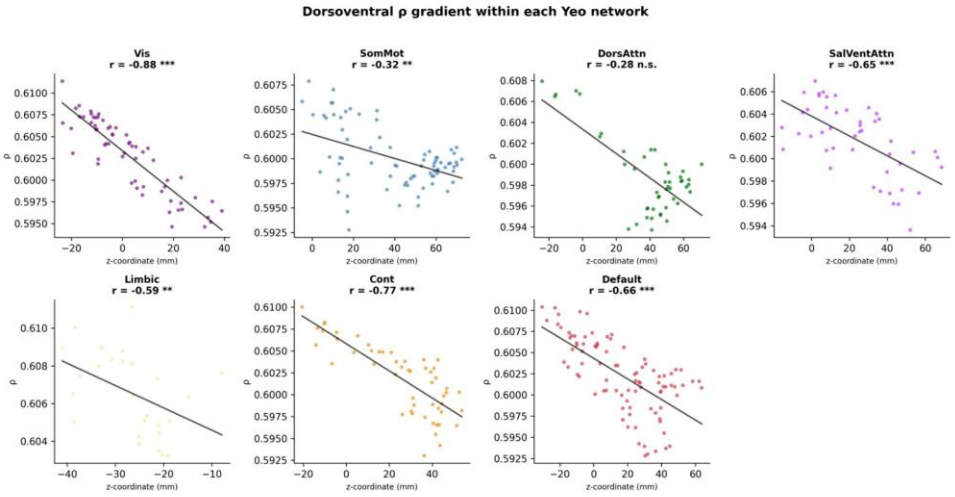
Fig. 4 | Excitatory–inhibitory balance model and interneuron gene expression.

a, E–I network model. Varying inhibitory gain (g_I) produces opposing effects on timescale τ (blue) and rotational index ρ (red), demonstrating that a single circuit parameter can generate the observed τ–ρ trade-off. b, Model-derived τ versus ρ across inhibitory gain values, coloured by g_I. The model produces a strong anticorrelation (r = −0.84, p = 0.0006), qualitatively matching the empirical τ–ρ trade-off. c, Spearman correlations between interneuron marker gene expression (Allen Human Brain Atlas) and ρ. SST shows a weak positive association (r = 0.12, p = 0.02) and PV−SST a weak negative association (r = −0.12, p = 0.02); neither survives spatial confound control. d–f, Scatter plots of ρ versus PVALB expression (d; r = −0.07, n.s.), SST expression (e; r = 0.12, p = 0.02), and PV−SST ratio (f; r = −0.12, p = 0.02).

Extended Data



Extended Data Fig. 1 | Spectral confound controls. Progressive partial correlation analysis demonstrating that the dorsoventral gradient of rotational dynamics survives control for spectral composition, total power, source depth and all confounds simultaneously.



Extended Data Fig. 2 | Within-network gradients. The dorsoventral gradient of rotational dynamics is present within six of seven Yeo functional networks (all |r| > 0.32; DorsAttn r = -0.28, n.s.), indicating that the gradient is not an artefact of network-level differences in mean rho.

xtended Data Tables

A dorsoventral gradient of rotational dynamics in human cortex

Extended Data Table 1. Validation against nonlinear measures.

Measure	r with ρ (mean ± s.d.)	r with z (DV)	Validates ρ gradient?
Spectral Entropy	+0.28 ± 0.14	+0.08	No (no DV gradient)
Sample Entropy	+0.16 ± 0.15	+0.18	No (opposite direction)
Permutation Entropy	+0.49 ± 0.17	−0.57	Yes (same DV gradient)

Extended Data Table 2. Gradient axis angles by region.

Metric	Region	Angle from DV	Angle from AP	Dominant axis
ρ	Full cortex	18°	72°	DV
ρ	Frontal	17°	73°	DV
ρ	Posterior	13°	78°	DV
τ	Full cortex	55°	37°	Mixed
τ	Frontal	6°	86°	DV
τ	Posterior	74°	24°	AP

Extended Data Table 3. τ–ρ correlations by region.

Region	τ–ρ raw (Spearman)	τ–ρ | z (Spearman)	Explanation
Full cortex	+0.34	−0.20	Frontal and posterior cancel
Frontal (y > 0)	+0.64	−0.05	Both axes DV → positive raw
Posterior (y ≤ 0)	+0.15	−0.37	Weaker raw; residual negative

Extended Data Table 4. Frequency-specific ρ gradients.

Band	Frequency	ρ–DV (r)	P (spin)	Direction
Delta	1–4 Hz	+0.55	< 0.001	Dorsal > Ventral
Theta	4–8 Hz	+0.47	< 0.001	Dorsal > Ventral
Alpha	8–13 Hz	−0.65	< 0.001	Ventral > Dorsal
Beta-low	13–20 Hz	−0.32	< 0.001	Ventral > Dorsal
Beta-high	20–30 Hz	−0.77	< 0.001	Ventral > Dorsal
Gamma-low	30–60 Hz	−0.73	< 0.001	Ventral > Dorsal
Broadband	1–40 Hz	−0.74	< 0.001	Ventral > Dorsal

Extended Data Table 5. Myelin independence.

Correlation	r	p	Interpretation
ρ vs myelin (MPC G1)	−0.03	0.49	No relationship
Myelin vs DV (z)	+0.07	0.16	Myelin has no DV gradient
ρ vs DV (raw)	−0.73	< 0.001	Main finding
ρ vs DV | myelin	−0.73	—	Unchanged after control

Notes: All correlations computed on Schaefer 400 parcellation (n = 400 parcels). P (spin) from spatial permutation testing (10,000 rotations). DV = dorsoventral axis (MNI z-coordinate). Table 3: frontal/posterior split by MNI y-coordinate (y > 0 vs y ≤ 0). Table 5: myelin proxy = BigBrain microstructure profile covaria